Arteriosclerosis, Thrombosis, and Vascular Biology

BASIC SCIENCES

Vascular Smooth Muscle Myosin 2 Filaments Dynamically Assemble and Stabilize During Induced Contractility

Sasha K. Demeulenaere,* Margaret A. Bennett,* Bradley Somerfield, Huini Wu, Margaret E. Utgaard, Hiral Patel, Stefano Sala, Elizabeth R. Longtine, Ahmed Zied, Jonathan A. Kirk, Patrick W. Oakes, Jordan R. Beach

BACKGROUND: Vascular smooth muscle cells (SMCs) dynamically tune blood vessel diameter to regulate blood pressure, provide vessel wall structural integrity, and absorb shock on a beat-to-beat timescale. SMII (smooth muscle myosin 2) is the dominant motor protein driving SMC contraction. To function, SMII monomers dynamically assemble into filaments, which associate with the actin cytoskeleton to drive contractility. Precisely how SMII filaments assemble and exchange in living SMCs, however, both at steady state and during induced contractility, remains poorly defined.

METHODS: We used a single-cell filament assembly assay to determine SMII assembly into filaments at steady state and upon induced contractility in rat aortic SMCs (A7r5) transiently expressing EGFP (enhanced green fluorescent protein)-tagged SM1A (SMII isoform 1A). We then used fluorescence recovery after photobleaching (FRAP) to characterize SMII exchange kinetics at steady state and upon induced contractility, and measured changes in force production using traction force microscopy. Finally, we developed a knock-in EGFP-SMII murine model to quantify SMII dynamics at endogenous expression in primary SMCs and intact arterioles.

RESULTS: While predominantly filamentous at baseline, induced contraction rapidly increased SMII filament assembly. Fluorescence recovery after photobleaching revealed rapid SMII exchange kinetics, more similar to nonmuscle myosin II than striated myosin II, and induced contractility consistently stabilized SMII filaments. Super-resolution imaging revealed SMII and nonmuscle myosin II filament structures consistent with coassembly. Endogenous EGFP-SMII in primary SMCs and intact arterioles paralleled cell culture studies with similar baseline exchange kinetics and activation-dependent stabilization.

CONCLUSIONS: Together, these data support a model in which SMII is surprisingly dynamic and coassembles with nonmuscle myosin II. Vascular SMC activation further increases SMII filament assembly while reducing filament exchange, consistent with stabilization of a dynamic SMII pool during force generation, thereby allowing cells to dynamically adapt their overall contractility in response to environmental conditions.

GRAPHIC ABSTRACT: A graphic abstract is available for this article.

Key Words: actins ■ blood pressure ■ muscle, smooth ■ myosin ■ phosphorylation

Smooth muscle is a fundamental component of the cardiovascular system. In arteries, the smooth muscle layer (tunica media) comprises a significant portion of the vessel wall and is dominated by vascular smooth muscle cells (SMCs). SMCs provide structural integrity and dynamically contract and relax to alter vessel diameter, thereby regulating vascular tone and blood pressure and absorbing pulsatile mechanical loads on a beat-to-beat timescale.[1] Contraction in SMCs is primarily powered by the dominant contractile protein SMII

Correspondence to: Jordan R. Beach, PhD, Department of Cell and Molecular Physiology, Stritch School of Medicine, Loyola University Chicago, 2160 S First Ave, Maywood, IL 60153. Email jbeach1@luc.edu
*S.K. Demeulenaere and M.A. Bennett contributed equally.
Supplemental Material is available at https://www.ahajournals.org/doi/suppl/10.1161/ATVBAHA.126.324897.

Arterioscler Thromb Vasc Biol is available at www.ahajournals.org/journal/atvb

Nonstandard Abbreviations and Acronyms

angII	angiotensin II
Cas9	clustered regularly interspaced short palindromic repeat–associated 9
FRAP	fluorescence recovery after photobleaching
GCaMP7s	green fluorescent protein calmodulin M13 peptide version 7s
IHM	interacting-heads motif
MLCK	myosin light chain kinase
NM2	non-muscle myosin 2
RLC	regulatory light chain
ROCK	Rho-associated coiled-coil containing protein kinase
SM1A	smooth muscle myosin 2 isoform 1A
SMC	smooth muscle cell
SMII	smooth muscle myosin 2

What Are the Clinical Implications?

SMII (smooth muscle myosin 2) is the principal contractile motor protein of vascular smooth muscle tissue, but its molecular behavior in living differentiated smooth muscle cells remains poorly defined. Here, we show that SMII is not a static contractile scaffold but highly dynamic. SMII exhibits dynamic exchange between the filament and monomeric forms at baseline but becomes acutely stabilized during agonist-induced contraction, including in primary smooth muscle cells and intact arterioles at endogenous *Myh11* expression. These findings suggest that vascular tone is tuned not only by activating preexisting myosin filaments but also by rapidly shifting SMII filament assembly levels and exchange rates. This framework is relevant to diseases in which smooth muscle cell contractility and arterial wall mechanics are abnormal, including *MYH11*-associated thoracic aortic disease and related disorders of arterial stiffness or maladaptive vasomotor regulation. Although this study is mechanistic, it identifies SMII filament dynamics as a measurable layer of vascular regulation and a potential readout for future studies of pathogenic *MYH11* variants, disease modeling, and therapies that alter myosin activation and cytoskeletal stability.

(smooth muscle myosin 2) acting on the actin cytoskeleton.[2] Consistent with SMII's central role in SMC contractile function, rare variants in SMII and other contractile proteins are linked to inherited aortic disease, including aneurysms and dissections.[3–5] SMC contractile function is, therefore, critical to vascular pathophysiology.

SMII is a member of the myosin 2 family, which also consists of striated myosin 2s (skeletal and cardiac) and NM2 (nonmuscle myosin 2).[6] All myosin 2 monomers are actually hexamers consisting of two dimerizing heavy chains, two essential light chains, and two RLCs (regulatory light chains). The extended coiled coil of the heavy chain can reversibly associate with other monomers in parallel and antiparallel fashion to enable the assembly of bipolar filaments with motor domains at opposing ends (Figure 1A).[7,8] These filaments are the functional units that interact with filamentous actin to drive contractile events. In SMCs, contractile activation is classically controlled by calcium-dependent and RhoA/ROCK (Rho-associated coiled-coil containing protein kinase)–dependent pathways that regulate myosin RLC phosphorylation.[9–11] Because SMII filament formation is reversible, the kinetics of exchange between monomer and filament-associated SMII pools can tune contractility on acute timescales.

Myosin 2 family members seem to modulate assembly dynamics and total assembly levels to differing extents. Here, we use the term assembly level to refer to the fraction of cellular SMII residing in filamentous structures versus the mobile monomeric pool. For example, non-muscle cells rapidly modulate non-muscle myosin 2 (NM2) filament assembly while maintaining about half of the total myosin 2 pool in filamentous form.[12,13] In contrast, striated myosin 2s assemble more stable filaments that generate contractile force independent of new filament assembly, with the vast majority of the total myosin 2 pool in filamentous form.[14] While significant contributions have been made to the field in recent decades,[15,16] we have less mechanistic insight into the molecular details of SMII filament assembly dynamics and activation than we do for striated and non-muscle myosin 2s. It has been suggested that SMC contraction primarily reflects activation of preassembled SMII filaments,[17] and assembly in tissue can be stimulated by changes in muscle length.[18] At the cellular level, SMII exists in both monomer and filament form,[19] however, and it is unclear whether SMII filaments in SMCs are stable (striated-like) or exchange dynamically (NM2-like), and how agonist activation modulates assembly and exchange. Considering that SMII is genetically similar to NM2, but perhaps more functionally similar to striated myosin 2s, which form stable filaments to drive repeated uniaxial contractile events, SMII behavior in cells is difficult to predict without experimentation.

A defining feature of vascular SMCs is their phenotypic plasticity, which enables adaptive tissue remodeling and repair in response to changing environmental cues. Vascular SMCs exist on a functional spectrum between a differentiated contractile phenotype and a more dedifferentiated migratory synthetic phenotype.[20,21] The differentiated phenotype is relatively stable and described as quiescent, whereas the dedifferentiated phenotype is characterized by increased proliferative and migratory ability. Previous studies have shown that SMCs can dedifferentiate rapidly in tissue culture.[22,23] Because

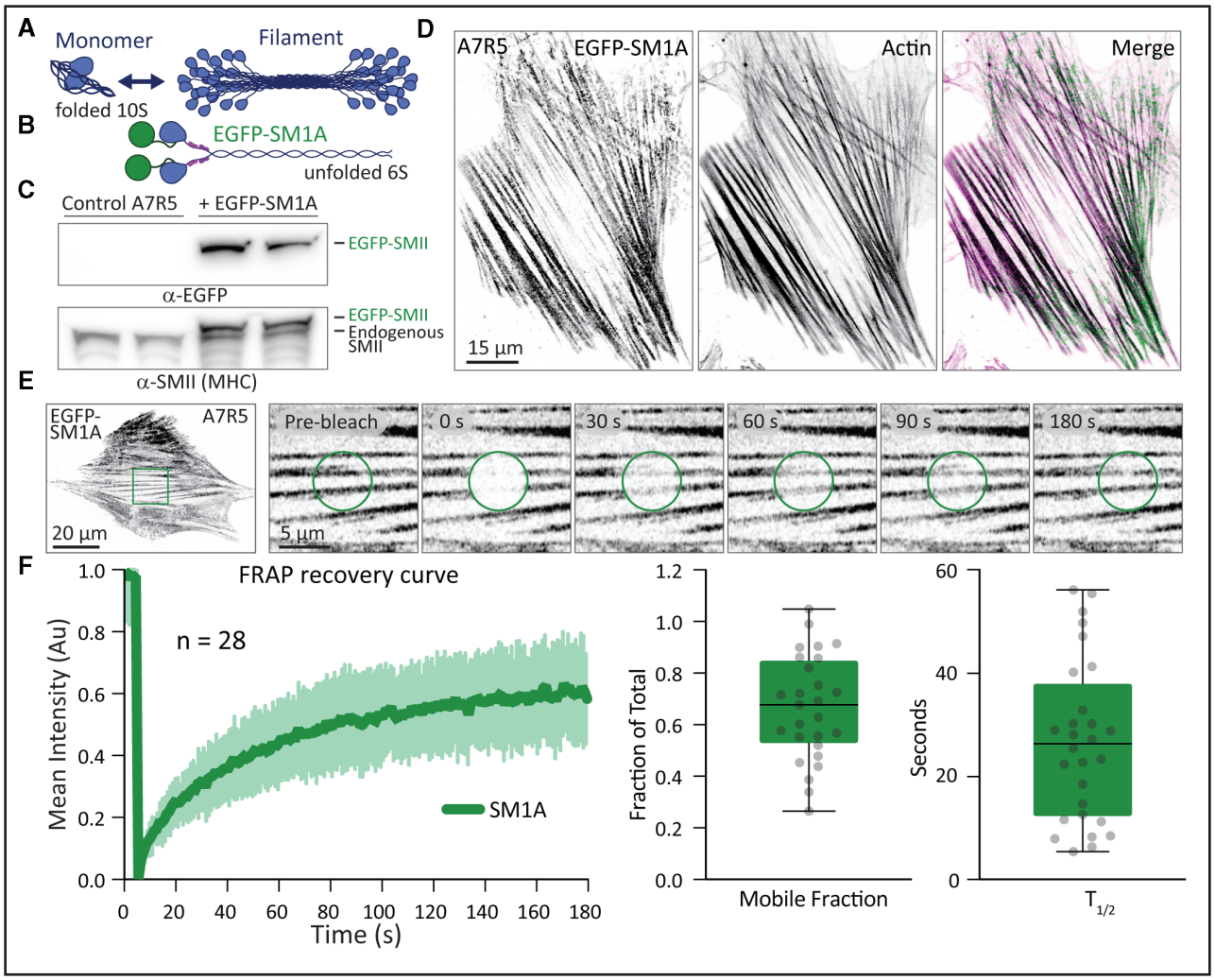

Figure 1. EGFP-SM1A filaments in A7r5 cells are highly dynamic.
A, Diagram of myosin 2 in folded monomeric and filamentous structural states. **B**, Diagram of an SMII (smooth muscle myosin 2) unfolded monomer tagged on the N terminus with EGFP. **C**, Duplicate Western blot of untransfected A7r5 (left lanes) and transiently expressing EGFP-SM1A (right lanes) probed with α-EGFP or α-SMII. **D**, Example images of an A7r5 cell transiently expressing EGFP-SM1A (green), fixed and stained with phalloidin (actin; magenta). **E**, Fluorescence recovery after photobleaching (FRAP) example of an A7r5 cell expressing EGFP-SM1A. Bleach region indicated by green circle in insets. **F**, Average FRAP recovery curve plotted for EGFP-SM1A for 28 cells from 3 independent experiments, along with mobile fraction and $t_{1/2}$ data displayed as box and whiskers (median±quartiles), calculated using a first-order exponential fit.

phenotype transitions can alter the expression, localization, and regulation of contractile proteins, measurements in standard in vitro models may not fully reflect SMII behavior in differentiated SMCs in vivo. Accordingly, investigating endogenous SMII in primary cells and intact tissue is ideal to define physiological assembly and exchange dynamics in their native context.

In this work, we define SMII filament assembly and exchange dynamics across cultured SMCs, primary SMCs, and intact arterioles using a new EGFP-SMII knock-in murine model that enables endogenous SMII imaging. In cultured rat aortic SMCs, the dominant vascular SMII isoform (SM1A [smooth muscle myosin 2 isoform 1A]) is predominantly filamentous at steady state but remains highly dynamic and likely coassembles with NM2. Agonist-induced contractility results in increased filament assembly and stabilized SMII exchange that parallel calcium signaling and cell-scale force production. In primary SMCs and intact arterioles, endogenous EGFP-SMII shows similar activation-dependent reductions in exchange, consistent with acute stabilization of the SMII filament pool during contraction. Together, these data support a model in which SMC activation induces both nascent SMII filament assembly and activation-dependent stabilization of preexisting filaments, providing a mechanism by which SMCs may tune vascular tone and wall mechanics in health and disease. Most models of vascular dysfunction currently emphasize upstream signaling, transcriptional state, or extracellular matrix remodeling rather than the dynamic behavior of the SMII

filaments that directly generate force. Defining SMII filament dynamics in healthy conditions lays the foundation for future efforts to understand how altered filament assembly or exchange could impair contractility, vascular tone, wall compliance, and the cellular response to biomechanical stress in pathological states.

MATERIALS AND METHODS

All data, analytic methods, and study materials will be made available for academic research upon reasonable request to the corresponding author. Detailed information for key reagents, cell lines, plasmids, animal models, and software is provided in the Major Resources Table.

Mammalian Expression Plasmids

To make pEGFP-SM1A (smooth muscle myosin 2 isoform 1A), a single gBlock was purchased from Integrated DNA technologies that contained the 5' 420 basepairs of human SM1A, including the naturally occurring Sal1 restriction site, a short 5 basepair linker to facilitate restriction enzyme digestion, and the terminal 3' 616 base pairs, including the naturally occurring Blp1 restriction site and a terminal stop codon. This dsDNA was inserted into pEGFP-C1 after digestion with Bgl2 and Kpn1 restriction enzymes. The internal coding sequence of *MYH11*, not included in the gBlock, was digested from full-length cDNA (MHS6278202857900; Horizon Discovery) with Sal1 and Blp1 (4911 basepairs) and ligated into the pEGFP-C1-SM1A intermediate following digestion with Sal1 and Blp1. To make pLVX-GCaMP7s (green fluorescent protein calmodulin M13 peptide version 7s), Janelia GCaMP7s (jGCaMP7s) was polymerase chain reaction amplified from pGP-CMV-jGCaMP7s (Addgene 104463). Following gel extraction, this dsDNA was inserted into the pLVX backbone with a CMV promoter using Gibson Assembly. GCaMP7s subject to polymerase chain reaction was sequence validated. NM2A-mApple (non-muscle myosin 2 isoform A tagged with monomeric Apple) contains an mApple fluorophore on the C terminus of NM2A and was described previously.[24]

Cell Culture, Transfections, and Transductions

Rat aortic SMC line, A7r5 cells, were obtained from ATCC and cultured in DMEM (MT10013CV, Corning) supplemented with 10% fetal bovine serum (MT35-010-CV, Corning) and 1% antibiotic-antimycotic solution (MT30004CI, Corning). At 24 hours before each experiment in Figures 1 through 3, A7r5 cells were transfected with 2-µg total pDNA using the lipid-based transfection system LipoD293 DNA transfection reagent (SL100668; SignaGen). For FRAP experiments in Figure 4, A7r5 cells were transduced with SM1A-adenovirus 48 hours prior at 1:2000.

The A7r5 cells used for traction force microscopy were treated with lentivirus expressing GCaMP7s. A GCaMP7s-positive population was obtained using fluorescence-activated cell sorting. Lentiviral production was performed in HEK-293-FT cells using psPAX.2 and pMD2.G with LipoD293 DNA transfection reagent. Lentiviral-containing media were collected at 48 and 72 hours, filtered, and directly used for transduction of A7r5 cells. Plasmid psPAX2 and pMD2.G were gifts from Didier Trono (Addgene plasmids 12260, 12259). A7r5 cells were induced toward the contractile phenotype using serum starvation, whereby plated cells previously grown in full (10% serum) were given either 0% serum, 2.5% serum, or the control 10% serum for 24 hours.[25]

Microscopy

Imaging was performed on the following systems. Figures 1, 2C and 2D, and 3A through 3C were acquired on a Zeiss LSM 880 Airyscan with a 63× 1.4 NA Plan-Apochromat objective in Airyscan Fast mode at 1× Nyquist sampling for optimal confocal resolution at 1 Hz for up to 1200 seconds. For FRAP experiments, a circular region (5 µm diameter) was bleached using 405-, 458-, and 488-nm lasers at 100% laser power. Figures 4, 5C and 5D, and 6 were acquired on a Yokogawa W1 Spinning Disk Confocal Microscope attached to a Zeiss Axiovert7 stand with the phasor spatial illumination system (Intelligent Imaging Innovations) with a 63× 1.4 NA Plan-Apochromat objective. For FRAP experiments, a 4-µm circular region was illuminated at 100% laser power using the 405-nm laser for 500 ms (cells) or 1500 ms (tissue). Figures 2A and 2B and 5F and 5G were acquired on a Zeiss SIM5 with a 63× 1.4 NA Plan-Apochromat objective. Scan Mode was FastFrame with 1.0× zoom, and reconstruction was performed with SIM^2. All live imaging was performed in environmental chambers to maintain temperature at 37 °C and 5% CO_2, while Definite Focus (Zeiss) was used to maintain the focal plane.

Single-Cell Assembly Assay

The single-cell assembly assay was performed on A7r5 cells transiently overexpressing EGFP-SM1A. Cells were plated in a 96-well coverglass-bottom dish (655891, Greiner). Total EGFP-SM1A signal was collected for 16 positions per well. If applicable, small molecules were added and cells incubated for the indicated time. Then, Triton buffer (5-µM PEG8000, 100-mmol/L PIPES, 150-mmol/L NaCl, 1-mmol/L EGTA, 1-mmol/L MgCl2, 0.5% Triton) was added to permeabilize the cells and release soluble EGFP-SM1A. The exact same positions were reimaged to collect the Triton-insoluble EGFP-SM1A signal. Individual cell masks were manually identified using FIJI. Local background fluorescence and mean fluorescence intensity were measured for each cell before and after permeabilization. Fraction assembled was then calculated as the background-subtracted signal post-permeabilization relative to the background-subtracted signal pre-permeabilization.

FRAP

FRAP was performed either on a Zeiss LSM 880 Airyscan (Figures 1 and 2) or a Yokogawa W1 Spinning Disk Confocal Microscope (Figures 4 and 6). See the microscopy section for additional details. For FRAP experiments on cells, an FRAP experiment was first performed in one region, dimethyl sulfoxide or a drug was added, and then, an FRAP experiment was performed in a new, unique region in the same cell. The delay between carbachol addition and initiation of the second FRAP time-course was 30 to 60 seconds. For FRAP experiments on arterioles within esophageal tissue, we performed control FRAP on a small region of an EGFP-SMII SMC embedded in an arteriole, followed by angII (angiotensin II) treatment and a

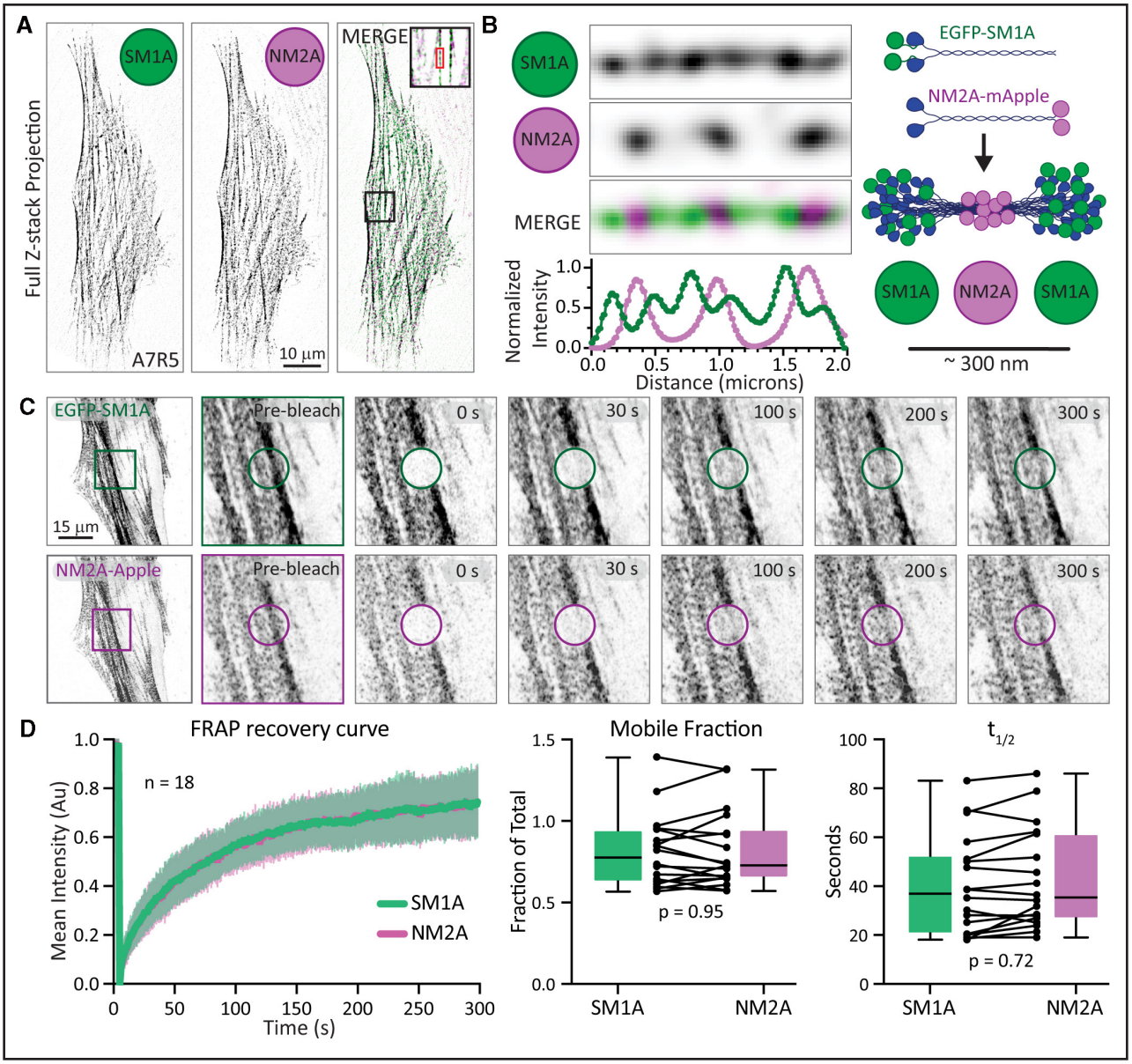

Figure 2. SM1A coassembles with NM2A.

A, A7r5 cells cotransfected with EGFP-SM1A and NM2A-mApple were imaged with SIM and sum projected. Individual channels are displayed in inverted gray scale, and the merge is shown in the right figure. **B**, An individual actomyosin fiber was cropped from the cell in **A** and displayed at higher zoom for SM1A, NM2 (nonmuscle myosin 2), and merge. The lower plot is a line scan through the fiber normalized to maximum intensity for each channel (left) diagram of coassembled EGFP-SM1A and NM2A-mApple (right). **C**, FRAP example of an A7r5 cell expressing EGFP-SM1A (top row) and NM2A-mApple (bottom row). Bleach regions indicated by circles. **D**, Average recovery curves of SM1A and NM2 plotted as mean±SEM for 18 cells from 3 independent experiments. Mobile fraction and $t_{1/2}$ are displayed as both box and whiskers (median±quartiles) and spaghetti plots. Dots in the spaghetti plot represent individual cells for NM2 and SM1A, with lines connecting cells. A paired *t* test was performed, and there was no statistically significant difference between groups.

second FRAP measurement after ≈2 minutes (to allow agonist penetration) on a neighboring SMC within the same arteriole. This provided vessel-specific internal controls to monitor relative changes in assembly dynamics. FRAP analysis was performed using a script written in Python similar to previous protocols.[26] Three ROIs were measured for each experiment: a bleach region, a control region within the cell, and a background region outside of the cell. Intensity was monitored over time in each region. Recovery within the bleach region was obtained after normalizing to the control region and subtracting the background region. Recovery curves were fit to a single exponential $I(t)=A*(1-e^{-kt})$, to determine the mobile fraction A and $kobs$. $t_{1/2}$ was subsequently calculated as $\ln 2/kobs$.

Immunocytochemistry

Cells were fixed using a 4% paraformaldehyde solution (15710; Electron Microscopy Sciences) in cytoskeletal buffer (0.1M MES, 0.03M MgCl2, 1.38M KCl, and 0.02M EGTA in 1 L H_2O) for 15 minutes at 37°C. The PFA solution was removed, and

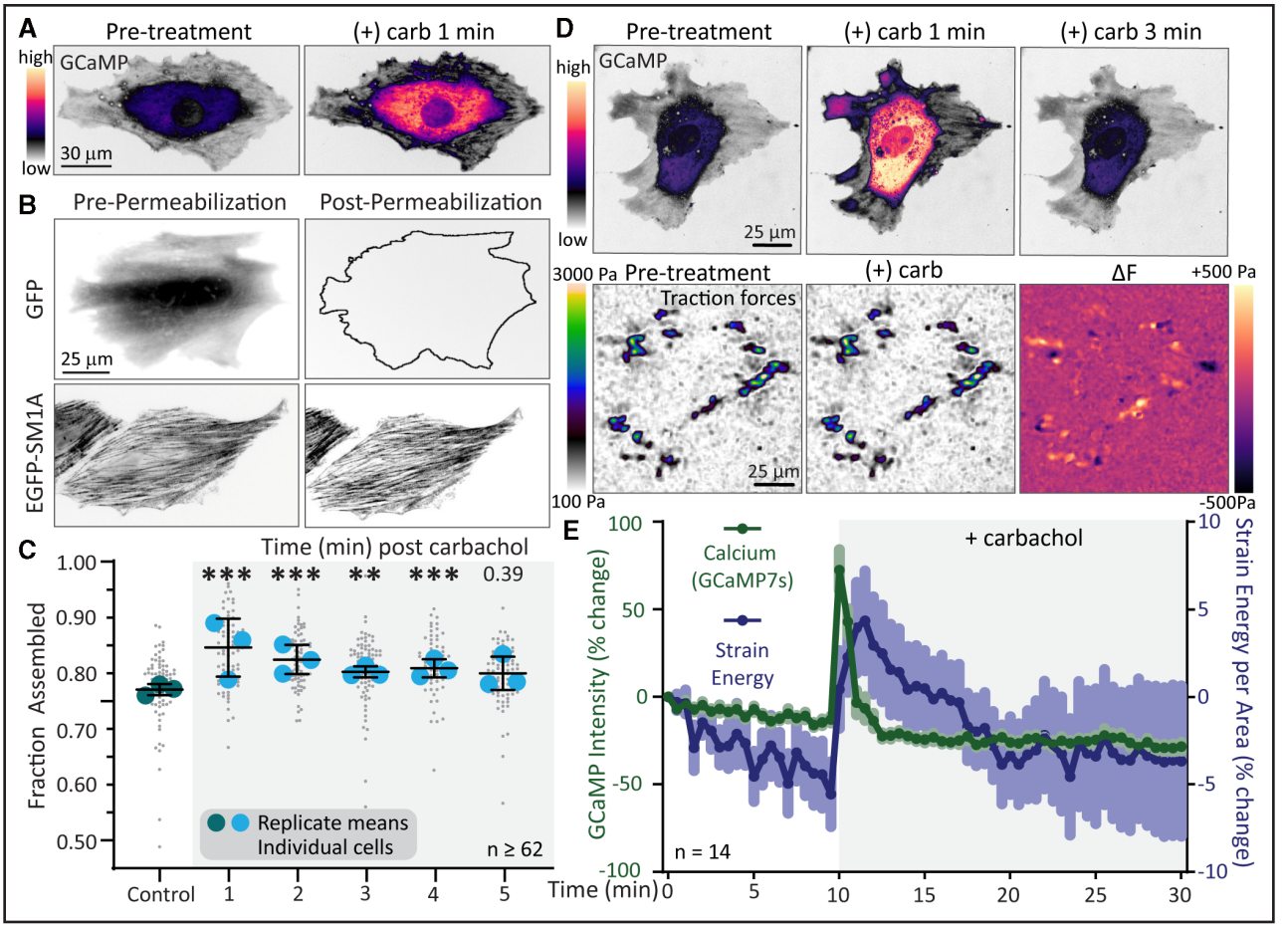

Figure 3. Induced contraction of smooth muscle cells (SMCs) drives SM1A assembly and a contractile response. **A**, A7r5 cell expressing GCaMP7s (green fluorescent protein calmodulin M13 peptide version 7s) was imaged pre- and post-addition of 10-µmol/L carbachol. GCaMP intensity is displayed with an inverted look up table (iLUT; scale on **left**). **B**, A7r5 cells expressing EGFP-SM1A were imaged live to determine total SM1A intensity. Cells were treated with or without 10-µmol/L carbachol for the indicated time, monomeric SM1A was extracted using a Triton buffer, and a second image was taken to determine the intensity of the remaining filamentous SM1A. As a control, A7r5 cells expressing free EGFP were imaged pre- and post-permeabilization to demonstrate that cytoplasmic proteins are fully extracted from the cell. **C**, Quantification of the fraction of SM1A assembled in control cells and cells treated with 10-µmol/L carbachol for the indicated time. Small circles indicate individual cells (n x≥y 62 per group). Larger colored circles indicate the means of 3 independent experiments. Because at least 1 group did not pass normality testing (Shapiro-Wilk test), groups were compared using a Kruskal-Wallis test with the Dunn multiple comparisons test comparing each carbachol-treated time point to control. *, **, and *** represent $P<0.05$, $P<0.01$, and $P<0.001$ respectively. **D**, An A7r5 cell expressing GCaMP7s was monitored for cytosolic calcium levels while simultaneously measuring its force production using traction force microscopy pre- and post-carbachol. Precarbachol and postcarbachol traction maps are the averages of the 10 minutes before and after carbachol treatment. The ΔF image represents postcarbachol-precarbachol average traction maps. **E**, Quantitation of the percent change of cytosolic calcium (green) and strain energy per area (blue) over time. Data plotted as mean±SEM for 14 cells from 3 experiments.

cells were rinsed with 1×PBS, permeabilized with a solution of 0.5% Triton X-100 (Fisher BioReagents) in cytoskeletal buffer for 15 minutes, rinsed in 1×PBS, and blocked with a solution of 10% goat serum in 1×PBS for 30 minutes. Fixed samples were incubated with primary antibodies at 4 °C overnight in 5% goat serum, washed in 0.05% Triton X-100 in 1×PBS for 3×10 minutes with gentle rocking, incubated in secondary antibodies diluted in blocking solution for 1 hour at room temperature, and washed in 0.05% Triton in PBS 3×10 minutes before imaging or mounting. Cells were mounted using ProLong Glass antifade mountant (P36980; Thermo Fisher). Mounted samples were allowed to cure for 18 hours in a dark drawer at room temperature before imaging.

A7r5 cells were stained expressing EGFP-SM1A, NM2-mApple and Alexa Fluor 405 phalloidin (A30104, Thermo Fisher). Primary EGFP-SMII SMCs were stained for NM2B (230823, AbCam) and phalloidin.

Western Blot

Cells were scraped, collected or pelleted, and resuspended in 2× sample buffer, boiled for 5 minutes, sonicated briefly, and used for analysis or stored at −20 °C. Tissues were weighed out to ≈30 to 50 mg, cut up into small pieces, resuspended in 2× sample buffer, boiled for 10 minutes, sonicated briefly, and used for analysis or stored at −20 °C. Proteins were separated on 4% to 20% gel, unless separation of EGFP-SM1A and SMII was required, in which case a 7.5% gel (cells) or 3% to 8% tris-acetate gel (tissues) was used. Protein was transferred to a polyvinylidene fluoride membrane using eBlot L1 (Genscript).

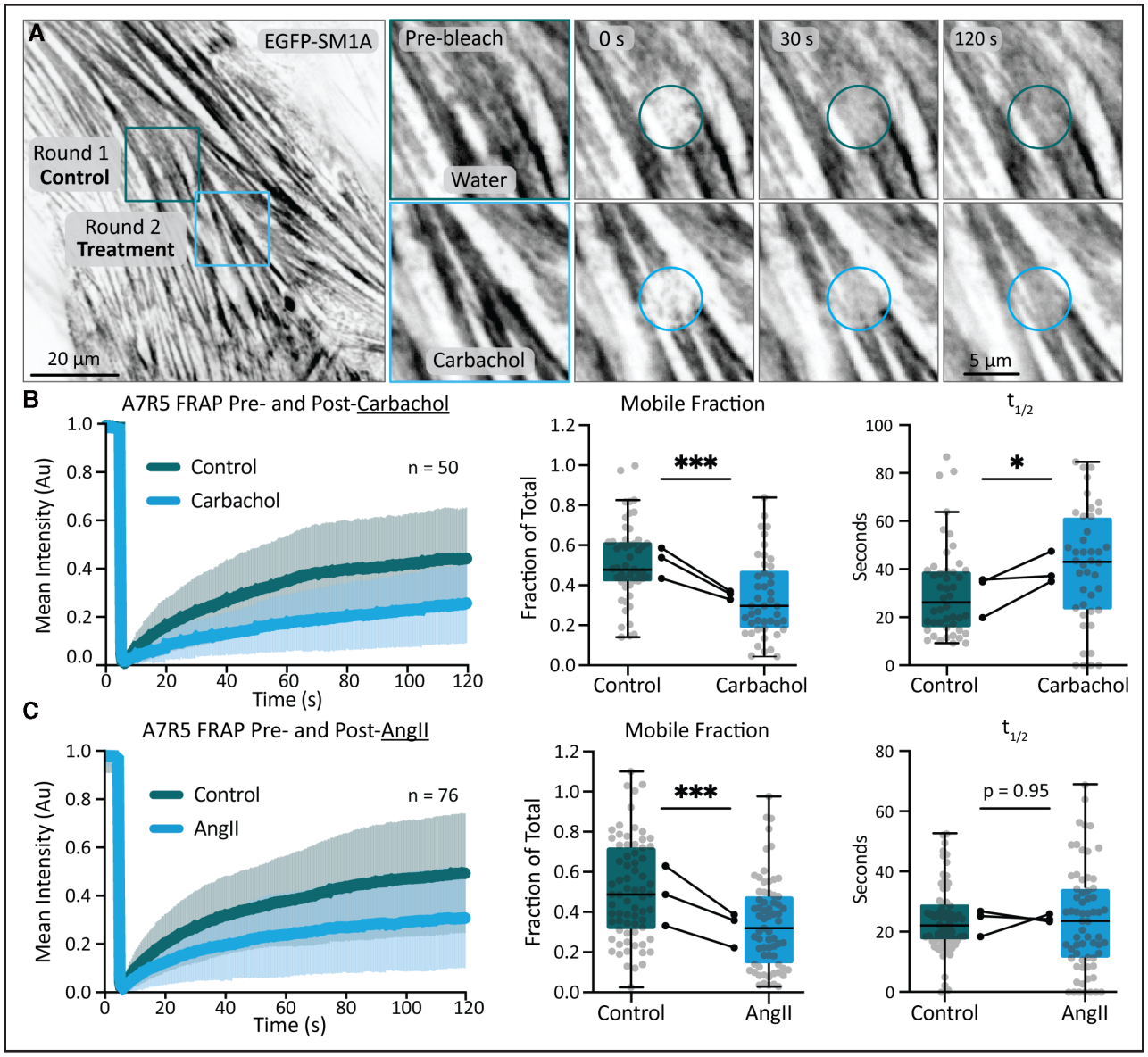

Figure 4. SM1A filament dynamics stabilize upon induced contraction.
A, Example fluorescence recovery after photobleaching (FRAP) experiment of a single cell before and after addition of calcium agonist. Fluorescence recovery of EGFP-SM1A in A7r5 pre-carbachol (green) and post-carbachol (blue). Circles indicate the bleach region. **B**, Mean recovery curves from 50 individual cells across 3 independent experiments. Mobile fraction and $t^{1/2}$ are reported with individual points in box and whiskers (median±quartiles). Means from each experiment are reported as dots in a spaghetti plot where precarbachol and postcarbachol measurements for individual experiments are connected. Paired *t* tests were performed on control and drug treatment cells when measuring mobile fraction, $t_{1/2}$. **C**, The same experiment as in **B** but using the agonist angII (angiotensin II). Data represent 76 individual cells from 3 independent experiments. * and *** represent $P<0.05$ and $P<0.001$, respectively.

Blocking was performed with 3% BSA in PBST (PBS+0.1% TritonX-100), and primary incubations were done overnight at 5°C. Primary antibodies were all used at 1:2000 in blocking buffer (SMII, Abclonal A4064; SMA, Abclonal A17910; EGFP, Santa Cruz SC-9996). Uncropped blots and loading controls are included in Figure S8.

Traction Force Microscopy

Traction force microscopy was performed as described previously[27,28] on the Spinning Disk (see the Microscopy section). Coverslips were prepared by incubating with a 2% solution of 3-aminopropyltrimethyoxysilane (313255000, Acros Organics) diluted in isopropanol, followed by fixation in 1% glutaraldehyde (16360, Electron Microscopy Sciences) in ddH20. Polyacrylamide gels (shear modulus: 16 kPa-final concentrations of 12% acrylamide [1610140, Bio-Rad] and 0.15% bis-acrylamide [1610142, Bio-Rad]) were embedded with 0.04-µm fluorescent microspheres (F8789, Invitrogen) and polymerized on activated glass coverslips for 1 hour at room temperature. After polymerization, gels were rehydrated overnight and coupled to human plasma fibronectin (FC010, Millipore) for 1 hour at room temperature using the photoactivatable crosslinker Sulfo-Sanpah (22589, Pierce Scientific).

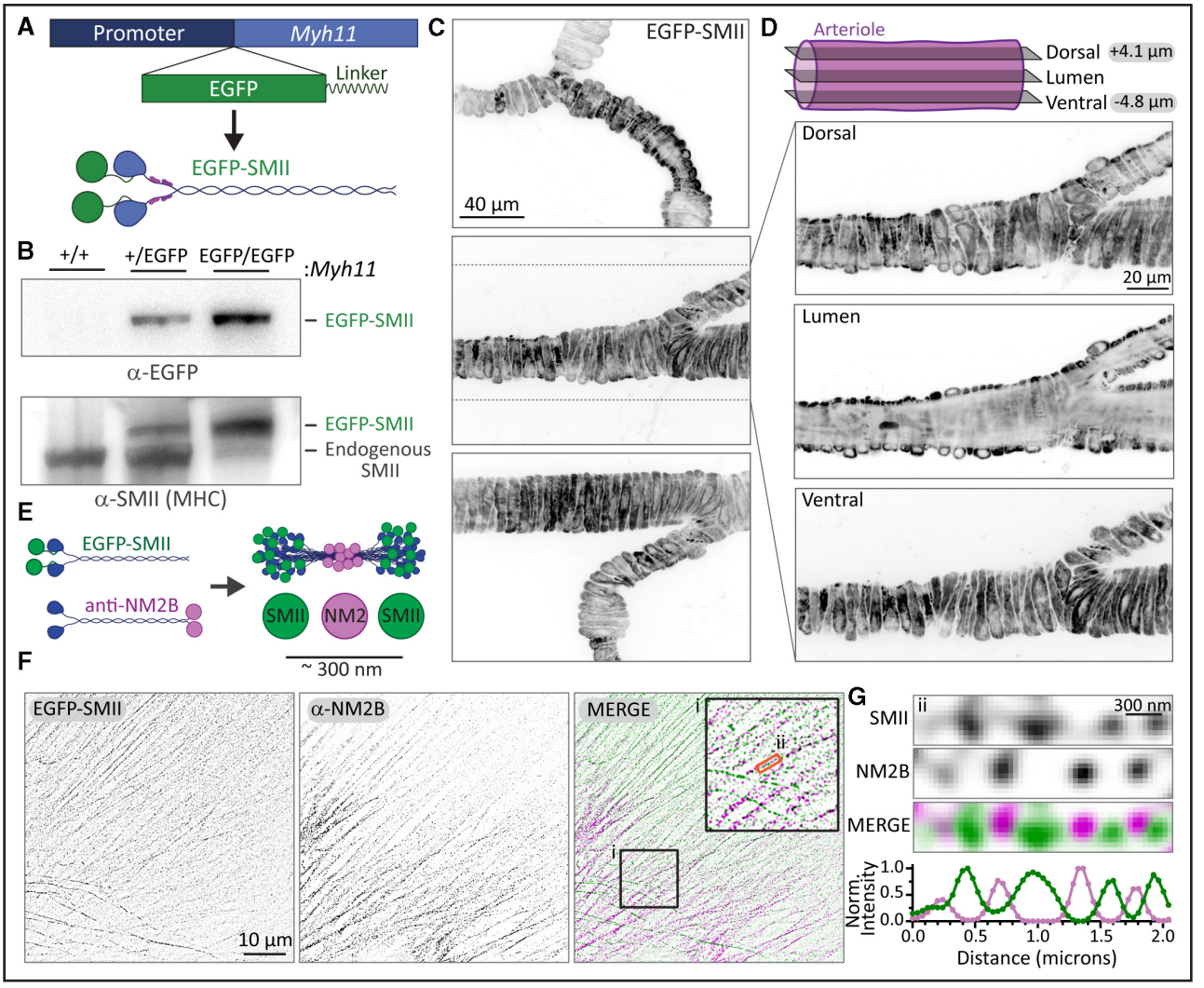

Figure 5. CRISPR-KI EGFP-SMII murine model reveals SMII and NM2 coassemble.
A, Diagram of CRISPR-KI EGFP-SMII murine model. **B**, Western blot of smooth muscle tissue from wild-type, heterozygote, and homozygote EGFP-SMII (N=3; 1F, 2M) mice probed with α-EGFP or α-SMII. **C**, Example images of isolated arterioles ex vivo expressing EGFP-SMII from homozygote mice (N=2; 1F, 1M). Images are max projections of confocal stacks. **D**, Example Z-stacks were taken longitudinally to demonstrate the intact cylindrical architecture. **E**, Diagram of coassembled EGFP-SM1A and NM2B, with the NM2B stained with a C-terminus antibody. **F**, Primary EGFP-SMII SMCs were isolated, immunostained for NM2B, imaged with SIM, and sum projected. **G**, An individual actomyosin fiber was cropped from the cell in **F** and displayed at higher zoom. The lower plot is a line scan through the fiber normalized to maximum intensity for each channel.

Following fibronectin crosslinking, cells were plated on the gels and allowed to adhere overnight. The next day, images were taken of both the cells and the underlying fluorescent beads. For kinetic analyses, images were collected every 30 s for 30 minutes. The first 10 minutes captured the steady state, then 10-μmol/L carbachol was added, and the cells were imaged for another 20 minutes. Immediately after imaging, cells were removed from the gel using 0.05% sodium dodecyl sulfate, and a reference image of the fluorescent beads in the unstrained gel was taken.

Analysis of traction forces was performed using code written in Python according to previously described approaches (available at https://github.com/OakesLab/TFM). Before processing, images were flatfield corrected and aligned to the reference bead image. Displacements in the beads were calculated using an optical flow algorithm in OpenCV (Open Source Computer Vision Library, https://github.com/opencv/opencv) with a window size of 8 pixels. Traction stresses were calculated using the FTTC approach, with a regularization parameter of 6.1×10^{-4}. The strain energy was calculated by summing one-half the product of the strain and traction vectors in the region under the cell[29] and normalized by the cell area as measured using the GCaMP7s image of the cell.

General Animal Maintenance and Welfare

All animal procedures were approved by the Institutional Animal Care and Use Committee at Loyola University Chicago and conducted in accordance with the National Institutes of Health Guide for the Care and Use of Laboratory Animals and Institutional guidelines. Mice were housed in individually ventilated cages under standard conditions (12-hour light/dark

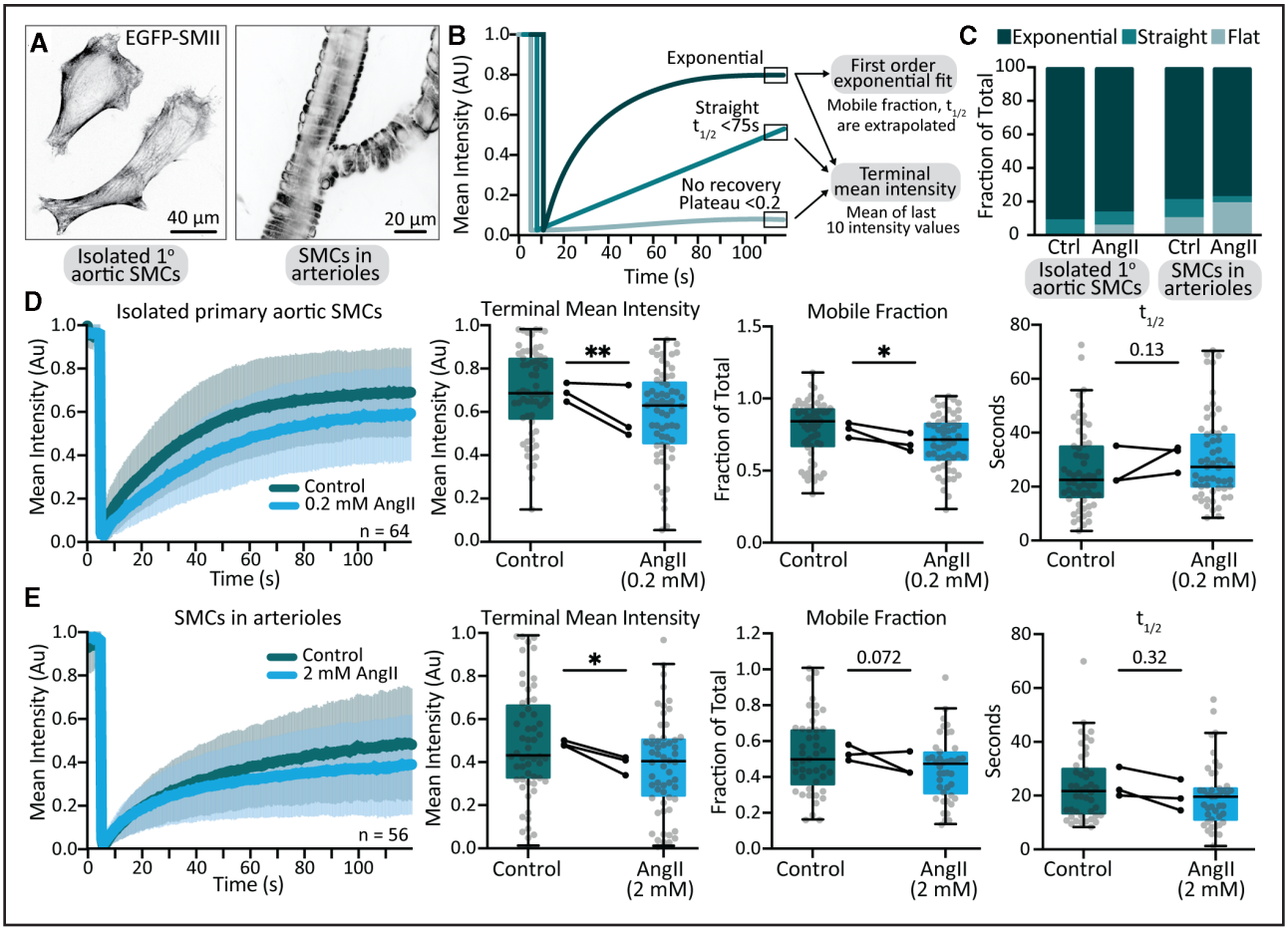

Figure 6. Induced contraction of primary SMCs stabilizes EGFP-SMII filaments.
A, Example images of primary EGFP-SMII isolated vascular SMCs (**left**) and whole arterioles ex vivo (**right**). **B**, Diagram representing the type of recovery curves we observed during fluorescence recovery after photobleaching (FRAP) experiments on primary SMCs (Figure S7) and the workflow for analysis. **C**, Stacked bar graph representing the fraction of recovery types (exponential, straight, and flat) we observed for each experimental group. **D**, FRAP experiments were performed on primary isolated EGFP-SMII cells (n=64). Mean recovery curves from 3 independent experiments are plotted (primary SMCs were isolated from N=3 animals; 2F, 1M). Mobile fraction and $t_{1/2}$ are reported with individual points in box and whiskers (median±quartiles). Means from each experiment are reported as dots in a spaghetti plot where pre- and post-angII (angiotensin II) measurements for individual experiments are connected. Paired *t* tests were performed in control and drug treatment cells when measuring mobile fraction and $t_{1/2}$. **E**, Repeat experiments were performed on SMCs (n=56) in whole arterioles ex vivo (N=3; 2F, 1M).

cycle), temperature, humidity, and with access to standard chow and water. Health status was monitored daily by trained animal care staff, and all procedures were performed with efforts to minimize the pain and distress of animals.

Generation of EGFP-SMII Knock-In Mice, Breeding, and Genotyping

Initial CRISPR/Cas9 (clustered regularly interspaced short palindromic repeats/clustered regularly interspaced short palindromic repeat–associated 9) knock-in was performed at the University of Chicago Transgenic Mouse Facility. C57BL/6J females were superovulated using the standard PMSG/HCG procedure. One-cell fertilized eggs were isolated on the day of injections. CRISPR/Cas9 components were delivered via pronuclear microinjection into 1-cell fertilized eggs. The ribonucleoprotein complex was prepared by annealing synthetic crRNA and tracrRNA (5'-CAGGGGACCACCAGACATCA-3' for *Myh11*; IDT) at a 1:1 molar ratio to form the sgRNA complex, which was subsequently incubated with Alt-R S.p. Cas9 nuclease (IDT) at room temperature for 20 minutes to ensure stable complex formation. The final injection mixture consisted of 25-ng/µL sgRNA, 100-ng/µL Cas9 nuclease, and 12.5-ng/µL donor plasmid DNA in cell culture grade ddH2O. The donor plasmid (pUC57-HA-EGFP-MYH11-Ms) consisted of a 705 bp 5' HDR of *Myh11* genomic sequence immediately upstream of the endogenous start codon (5'-TATGTGAGTA...ACCAGACATC-3'), an HA tag, a short 7 amino acid GS-rich linker, mEGFP, a linker, an 11 amino acid linker, and 714 bp 3' HDR of *Myh11* genomic sequence (5'-ATGGCGCAGA...CTCTGCCATG-3'). Following microinjection into the male pronucleus, surviving embryos were cultured briefly and then surgically transferred into the oviducts of pseudopregnant recipient females to allow for gestation and birth of founder mice. Founder mice were screened for EGFP insertion and bred out to screen for germline transmission.

The EGFP-SMII knock-in line was expanded by breeding the founders with wild-type C57BL/6J mice and subsequently bred to homozygosity. To reduce background variability, the line was backcrossed for 5 generations before the establishment of homozygote animals. Genotyping was performed using ear-clip tissue obtained at weaning. Ear clips were digested using an acid-based lysis/digestion method (25-mmol/L NaOH, 0.2-mmol/L EDTA pH 12 at 95 °C for 30 minutes, and neutralized with 40-mmol/L Tris-HCl pH 5 on ice) followed by polymerase chain reaction with primers flanking the integration site (Figure S5). Polymerase chain reaction products were analyzed by agarose gel electrophoresis to identify wild-type, heterozygous, and homozygous genotypes.

Body Weight, Blood Pressure, and Echocardiography

To assess baseline cardiovascular phenotype in our novel murine model, measurements were performed at 1 year of age to increase sensitivity for detecting genotype-associated differences in blood pressure and cardiac function. Body weights were recorded. Noninvasive systolic and diastolic blood pressures were measured in conscious mice using a tail-cuff volume-pressure recording system (Kent Scientific CODA Monitor), in accordance with the American Heart Association recommendations for experimental animal blood pressure measurement. Tail-cuff measurement was selected because blood pressure was used as a noninvasive baseline screen for major genotype-associated cardiovascular abnormalities, rather than as a primary end point requiring continuous blood pressure load assessment by telemetry.

Mice were acclimated to the procedure, restraint holders, warming platform, and tail-cuff measurements for 2 to 3 consecutive days before data acquisition. Blood pressure recordings were performed during the light cycle between 9 AM and 1 PM, and all mice were tested in the same room, with the same platform, temperature, and handling conditions. On each recording day, each mouse underwent 5 acclimation cycles followed by 15 measurement cycles per session. Systolic and diastolic blood pressures for each mouse were calculated from the mean of 15 accepted cycles per session.

Cycles were accepted only when the CODA software identified a valid volume-pressure recording trace, and there was no clear technical artifact, including tail movement or displacement, loss of cuff positioning, inadequate tail blood-flow signal, or cuff/sensor failure. Individual cycles were not excluded on the basis of high or low blood pressure values alone. A session was excluded only if <10 technically acceptable cycles were obtained after 2 attempted cycles. Mice were tested in randomized order with respect to genotype and sex, and the technician performing and analyzing the measurements was blinded to genotype. No animals were excluded. Transthoracic echocardiography was performed using a high-frequency Vevo 3100 ultrasound system. Mice were anesthetized with inhaled isoflurane and maintained on a heated platform with continuous monitoring of temperature, heart rate, and respiration. Left ventricular systolic functions, including ejection fraction, and mitral valve inflow parameters were quantified from standard parasternal long- and short-axis views and Doppler recordings using M- and B-mode imaging. Analyses were performed using Vevo LAB ultrasound analysis software.

Isolation and Culture of Primary EGFP-SMII Vascular SMCs From Aorta

To isolate primary EGFP-SMII SMCs, homozygous EGFP-SMII mice (12–16 weeks of age, male and female) were administered deep anesthesia followed by exsanguination. Briefly, the abdominal cavity was opened, the inferior vena cava was transected, and 1×PBS was perfused via the left ventricle until effluent cleared. The thoracic aorta was dissected under a dissecting microscope, and surrounding adipose and connective tissue were removed. The aorta was minced into small fragments and incubated in collagenase solution (collagenase type I, 10 mg/mL in PBS; Sigma-Aldrich, C0130) for 2 hours at 37 °C. Following digestion, tissue was pelleted by centrifugation (400 rcf, 4 minutes), resuspended in vascular SMC growth medium (C-22062, PromoCell), and passed through a 70-µm cell strainer (352350, Falcon). Cells were plated in 35-mm dishes and maintained at 37 °C in 5% CO_2. Medium was changed after 48 hours; cells were used for experiments after 72 hours and passaged as needed. To limit phenotypic drift, primary SMCs were discarded after passage 4.

Ex Vivo Arteriole Preparation and Imaging

For ex vivo arteriole imaging, the esophagus was carefully dissected from homozygous EGFP-SMII mice (12–16 weeks of age, male and female), opened longitudinally, and splayed flat on a glass coverslip using a tissue harp in media (641419, Warner Instruments). Arterioles within the esophageal tissue were identified by confocal microscopy based on vessel morphology and EGFP-SMII signal. Tissues were maintained at 37 °C, 5% CO_2 in the microscope humidity chamber, and imaged within 3 hours of euthanasia to minimize time-dependent loss of tissue viability. Bladder, colon, and uterus were also dissected from animals and flash frozen or processed for Western blots (as described earlier).

Statistical Analyses

Statistical analyses were performed using GraphPad Prism, version 11.0.2. Numbers of independent experiments, n values, and numbers of animals are reported in the corresponding figure legends. Data are displayed as described in each figure legend, including mean±SEM for time-course traces, single-cell plots showing median and interquartile range for single-cell distributions, and mean±SD for animal-level cardiovascular measurements. All tests were 2-sided, and $P<0.05$ was considered statistically significant. Asterisks indicate statistical significance as follows: $^{*}P<0.05$, $^{**}P<0.01$, and $^{***}P<0.001$.

Before applying parametric tests, data were assessed for normality using the Shapiro-Wilk test. For paired comparisons (SMII-NM2 coassembly FRAP and agonist activation experiments), normality was assessed using the paired differences; paired differences across all experiments displayed normality. Homogeneity of variance was not applicable for paired comparisons because these analyses compared matched measurements within the same cell or arteriole.

For the single-cell SMII assembly assay in Figure 3C and the data in S1 (assembly and FRAP), differences across groups were analyzed using ordinary 1-way ANOVA followed by the Dunnett multiple comparisons test, unless 1+ groups did

not satisfy the normality assumption, in which case the Kruskal-Wallis test with the Dunn multiple comparisons test was used instead.

Categorical FRAP recovery-class distributions were analyzed using contingency tables containing the number of traces classified as no/flat recovery, linear/straight recovery, or exponential recovery. Because some expected cell counts were <5, recovery-class distributions were compared using the Fisher exact test for a 3×4 contingency table rather than relying on the χ^2 approximation.

Cardiovascular measurements were analyzed separately by sex and outcome. Wild-type, heterozygous EGFP-SMII, and homozygous EGFP-SMII mice were compared using 1-way ANOVA analyses. Normality was assessed using the Shapiro-Wilk tests, and homogeneity of variance was assessed using the Brown-Forsythe tests. Data satisfying assumptions of normality and homogeneity of variance were analyzed using ordinary 1-way ANOVA followed by the Dunnett multiple comparisons test comparing heterozygous and homozygous EGFP-SMII mice to wild-type controls. Outcomes that did not satisfy normality were analyzed using Kruskal-Wallis tests with the Dunn multiple comparisons test versus wild-type; all outcomes satisfied homogeneity of variance.

RESULTS

SM1A and NM2 Filaments in Cultured SMCs Have Dynamic Exchange Kinetics and Likely Coassemble

A single gene (*MYH11*) produces 4 dominant SMII splice variants (SM1A, SM1B, SM2A, and SM2B) that vary in the presence or absence of splice inserts in the motor domain or C-terminal tail.[30] The dominant isoform in vascular SMCs is SM1A.[31,32] Therefore, to better understand the assembly dynamics of SMII filaments in SMCs, we generated an expression plasmid with an EGFP coupled to the N terminus of the SM1A heavy chain (EGFP-SM1A; Figure 1B). Western blot analysis of transient overexpression of EGFP-SM1A in A7r5 demonstrated expression of the EGFP-SM1A shifted above endogenous SMII, as expected (Figure 1C). High-resolution imaging demonstrated that EGFP-SM1A is associated with large actin stress fibers in cells (Figure 1D). Therefore, our EGFP-SM1A plasmid appears to be a faithful reporter of SM1A in these immortalized SMCs.

To investigate SMII filament exchange kinetics, we performed FRAP on A7r5 expressing EGFP-SM1A. Here, we use the term exchange to refer to the movement of myosin 2 monomers into and out of filaments and avoid the term turnover, which might also refer to protein synthesis and degradation and should not be relevant during our experimental timescales of a few minutes. Figure 1E shows an example FRAP experiment, with insets showing EGFP-SM1A before bleaching and during recovery. EGFP-SM1A displayed a relatively high fraction of the exchanging pool (mobile fraction ≈70%) and a low time for half of the exchange to occur ($t^{1/2}$≈30 s) relative to striated myosin 2 paralogs[33,34] (Figure 1F). This suggests that SM1A is capable of forming highly dynamic filaments in SMCs that are more reminiscent of nonmuscle myosin systems[12,13] than striated muscle myosin systems.[33,34]

As SMCs express both myosin 2 paralogs,[35] we sought to carefully investigate their relationship in our cell model. We coexpressed EGFP-SM1A and NM2A-mApple in A7r5 cells and observed extensive overlap in filamentous structures throughout the cell (Figure 2A). Closer examination of individual fibers revealed distinct alternating patterns of the 2 fluorophores (Figure 2B). Because each paralog is tagged with its respective fluorophore at opposing ends of the monomer (N and C termini; Figure 2B), this arrangement suggests that the SM1A and NM2A are coassembling into filaments in the SMCs, as has been seen previously for NM2 isoforms.[24,36] The alternating SM1A-NM2A-SM1A (green-magenta-green) patterns are also ≈300 nm in length (Figure 2B), consistent with what would be seen in coassembled filaments.

We next asked if SM1A and NM2A in the same filamentous networks had similar exchange kinetics. We performed simultaneous FRAP in A7r5 cells expressing both EGFP-SM1A and NM2A-mApple (Figure 2C). Our analysis revealed indistinguishable mobile fractions and $t^{1/2}$ values (Figure 2D), indicating that both SM1A and NM2A filaments exchange rapidly and readily when coexpressed in these cells. For SM1A, the exchange kinetics were similar regardless of NM2A expression (Figures 1F and 2D), suggesting that NM2 is not inducing a more dynamic SM1A. Collectively, then, SMII filaments in cultured SMCs display rapid polymer exchange kinetics that are indistinguishable from NM2 and colocalize with NM2 in filamentous structures in a manner consistent with coassembly.

A7r5 Cells Assemble New SMII Filaments and Display Calcium-Mediated Contractile Response to Carbachol

Because A7r5 cells in culture are likely closer to a dedifferentiated SMC phenotype with reduced contractile capacity, we first sought to confirm that they could still increase their contractility in response to an agonist. We performed control experiments with the acetylcholine receptor agonist carbachol, a cholinergic receptor agonist that stimulates the release of intracellular calcium via inositol trisphosphate.[37] In GCaMP7s-expressing A7r5 cells, carbachol elicited transient increases in cytosolic calcium (Figure 3A).

To determine if this calcium release produced SMII assembly, we performed a single-cell imaging-based Triton permeabilization assay to measure populations of monomeric and filamentous SMII in cells treated with or without carbachol (Figure 3B and 3C).[38] Comparing

intensity differences pre- and post-Triton enables quantitative determination of monomer/filament ratios on a single-cell basis. Control experiments with A7r5 cells expressing free EGFP reveal a complete loss of EGFP signal upon Triton permeabilization, demonstrating that cytosolic proteins are completely liberated in this assay (Figure 3B). Control assembly levels for SM1A at baseline were ≈75% filamentous (Figure 3C; Figure S1D). One minute after carbachol treatment, however, assembly levels increased by ≈10% and then decreased toward steady-state levels in the ensuing minutes (Figure 3C). We did not observe any obvious changes in SMII-NM2 coassembly upon carbachol treatment (Figure S2), nor did we observe any correlation between assembly and SMII intensity before permeabilization, suggesting that the increase in assembly we observed with induced contractility was not affected by the expression level of exogenous EGFP-SMII (Figure S3).

In parallel, we performed traction force microscopy to determine if these cytosolic calcium and SMII assembly increases were harnessed into contractile energy. We observed contractile force generation following carbachol treatment with a slight delay and extended duration relative to the cytosolic calcium response (Figure 3D and 3E), consistent with the calcium/MLCK (myosin light chain kinase)–dependent signaling cascade that displays similar kinetics in intact smooth muscle tissue.[39] Together, these data show that A7r5 cells mount a Ca^{2+}-dependent response to carbachol that is accompanied by a transient increase in SMII filament assembly and measurable contractile activity.

SM1A Filament Dynamics Are Stabilized Upon Transiently Induced Contraction

To determine if the increase in SMII assembly upon SMC-induced contractility is accompanied by a change in filament exchange kinetics, we performed FRAP on a small region of an A7r5 cell expressing EGFP-SM1A, then treated with carbachol, and rapidly (within ≈1 minute) performed FRAP on a similar but distinct region of the same cell (Figure 4A). This provided cell-specific internal controls to monitor relative changes in assembly dynamics. Upon SMC activation, we observed a consistent decrease in mobile fraction and a slight increase in $t^{1/2}$, consistent with stabilization of the SMII machinery (Figure 4B). To further validate our observed response to carbachol, we repeated the assay with an alternative agonist, angII, which stimulates SMC contractility via angII receptor–mediated calcium release.[40] We again observed a significant decrease in the mobile fraction but with less impact on $t^{1/2}$ (Figure 4C). Together, internally controlled FRAP measurements show that agonist stimulation (carbachol or angII) consistently reduces the SMII mobile fraction, likely indicating stabilization of the SMII filaments during induced contractility.

SMII Exchange Kinetics and Assembly Are Unchanged Upon Differentiation of A7r5

As SMCs are known to dedifferentiate in vitro, we sought to determine whether SM1A assembly dynamics were altered upon induction of the differentiated phenotype via serum starvation of A7r5s.[41] Expression of contractile proteins in cells under various serum conditions shows that serum starvation increases both SMII and smooth muscle actin, confirming that cells were pushed toward the differentiated phenotype (Figure S1A and S1B). FRAP analysis, however, revealed that SM1A exchange kinetics were not significantly altered, as there was no noticeable difference in mobile fraction or $t^{1/2}$ between serum-starved or nonserum-starved cells (Figure S1C). In our assembly assays, we also observed no significant difference in the steady-state assembled fraction between serum-starved and nonstarved conditions (Figure S1D). Together, these results suggest that while serum starvation increases expression of contractile markers and promotes a slightly more differentiated A7r5 phenotype, baseline SM1A filament assembly and exchange kinetics remain largely unchanged under these conditions.

Establishment of an EGFP-SMII Murine Model

While our data in A7r5 cells provide valuable insight into SMII assembly and exchange, SMC stable cell lines in culture are prone to phenotypic drift, and these measurements likely reflect SMII behavior in a more dedifferentiated state. To determine whether the same SMII organization and dynamics are preserved at endogenous expression in primary SMCs and intact tissue, we generated a knock-in mouse using CRISPR/Cas9 in which EGFP is fused in-frame to the N terminus of the endogenous *Myh11* locus (Figure 5A). As the splice variants do not use alternative translation start sites, this strategy labels all 4 major splice variants and tags SMII in all SMCs in the organism (Figure S4). Correct targeting and expression were confirmed by genotyping (Figure S5) and Western blot analysis. Western blot analysis detected the EGFP-SMII fusion protein in heterozygous and homozygous animals and demonstrated the expected allele-dependent shift from endogenous SMII to the higher molecular weight EGFP-SMII species (Figure 5B). In intact arterioles in tissue explants, EGFP-SMII signal exhibited the expected circumferential/longitudinal filament architecture across the vessel wall, and optical sectioning highlighted consistent labeling across the dorsal, lumen, and ventral planes (Figure 5C and 5D), supporting robust incorporation of the tagged SMII protein into native contractile structures. Finally, super-resolution SIM imaging in primary SMCs revealed that SM1A head domains are about 300 nm apart, flanking NM2 isoform B (NM2B) tails, again suggesting coassembly of EGFP-SMII with nonmuscle

myosin II (Figure 5F and 5G). Mouse weights, blood pressures, and echocardiographs were taken to characterize cardiovascular health at 1 year of age (Figure S6). No significant differences were detected between wild-type, heterozygote, and homozygote EGFP-SMII animals, suggesting that the EGFP-SMII does not alter cardiovascular physiology. Together, these validation data establish the EGFP-SMII knock-in mouse as a physiologically relevant platform to quantify SMII assembly, exchange kinetics, and higher-order organization in primary differentiated SMCs and intact vascular tissue.

SMII Filament Dynamics in Primary SMCs and Arteriole Tissue Are Stabilized Upon Transiently Induced Contraction

To evaluate whether the changes in SM1A filament dynamics we observed with transiently induced contraction in A7r5s were present in SMC physiologically, we repeated FRAP experiments on isolated primary SMCs and intact arterioles from EGFP-SMII knock-in mice (Figure 6A). We performed paired control FRAP experiments on either the same primary SMC in culture or a neighboring SMC within the same arteriole before and after angII treatment, thus providing cell- or vessel-specific internal controls to monitor relative changes in assembly dynamics.

Compared with A7r5 cells, FRAP recovery curves in primary SMCs in culture and in tissue explants were more heterogeneous and frequently deviated from a simple single-exponential profile. Across conditions, recovery traces fell into 3 reproducible classes: (1) no recovery, (2) linear recovery, and (3) exponential recovery, which we subsequently analyzed (Figure 6B). First, recovery distributions differed across the 4 experimental groups (the Fisher exact test for a 3×4 contingency table; P=0.0043), with AngII treatment showing a higher fraction of linear/no recovery (Figure 6C), suggestive of a shift toward a more stable SMII filament during transiently induced contraction. Next, we sought to compare all 3 types of recovery curves across the population with the same analysis. Because $t^{1/2}$ and mobile fraction are only well-defined for exponential recoveries, we quantified the terminal mean intensity (mean of the final 10 time points) for all FRAP measurements. Terminal mean intensity decreased following angII treatment in both isolated SMCs and arterioles (Figure 6D and 6E), consistent with reduced SMII exchange. Finally, we analyzed the mobile fraction and $t^{1/2}$ on recovery curves that could be fit with an exponential. This once again resulted in a decreased mobile fraction but no significant change in $t^{1/2}$ (Figure 6E), supporting activation-dependent stabilization of the SMII machinery in both isolated primary SMCs in culture and in intact arterioles.

DISCUSSION

Our research supports an updated model of SMII filament exchange, assembly, and contraction (Figure 7). At steady state, SMII is predominantly filamentous yet remains highly dynamic, exchanging with the monomeric pool, and exhibits the ability to coassemble with NM2. Across cultured rat aortic A7r5 cells and primary

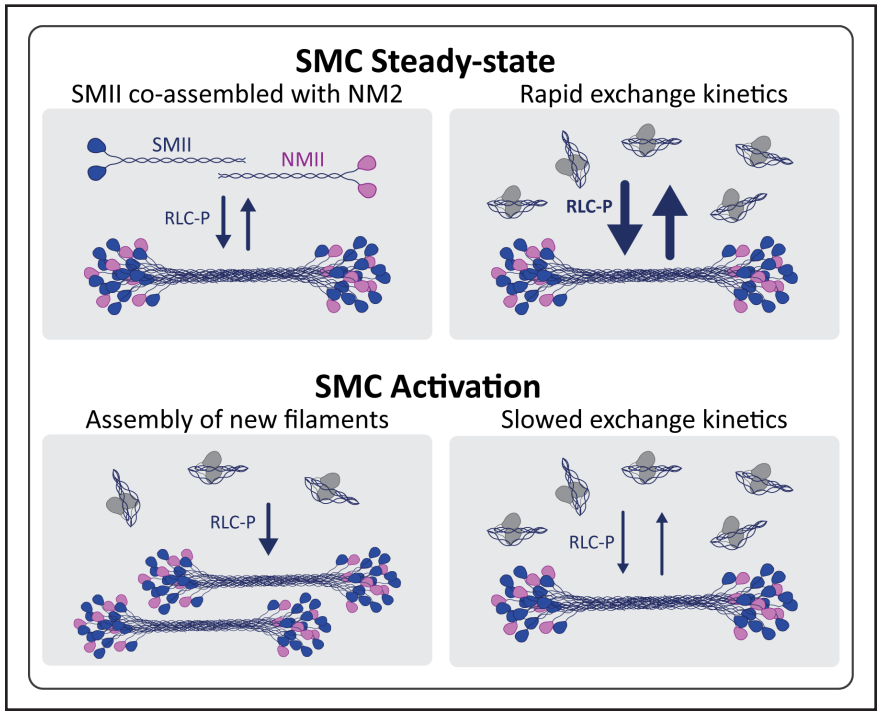

Figure 7. Model of SMII assembly at steady state and upon activation. See the Discussion section for a description. NM2 indicates nonmuscle myosin 2; RLC-P, regulatory light chain phosphorylation; and SMC, smooth muscle cell.

SMCs and intact arterioles isolated from our EGFP-SMII knock-in mouse, agonist stimulation stabilizes SMII filaments, reduces SMII exchange, and increases filament assembly. Collectively, this enhanced assembly and stabilization of SMII then increase SMC contraction.

To increase total assembly levels of myosin 2 filaments, one could increase the rate at which monomers are added (on rate) or increase the dwell time in which monomers stay in the filament, or both. To increase the on-rate, the most likely scenario is that MLCK-mediated RLC phosphorylation drives the folded, autoinhibited monomer (10S) to open into the assembly-competent form (6S), which then readily incorporates into filaments (Figure 7). This model is well-supported by the literature.[18,19,42] To increase the dwell time, we speculate that MLCK is acting upon filamentous SMII. In theory, SMII monomers assembled into filaments could exist with 0, 1, or 2 RLCs phosphorylated, and importantly, only 1 phosphorylated RLC is required to activate the complex.[43,44] While an SMII with 0 phosphorylated RLCs might be prone to disassembly and a return to the folded 10S, early studies suggested that as much as ≈85% of SMII in smooth muscle was filamentous in relaxed smooth muscle, but only ≈5% of the RLC was phosphorylated.[45] Therefore, the existence of unphosphorylated SMII monomers in filaments is likely. MLCK phosphorylation of monomers with 0 or 1 phosphorylated RLCs should extend monomer dwell time in the filament, thereby decreasing the off-rate and increasing total assembly levels. In parallel, this model of enhancing RLC phosphorylation of filamentous myosin 2 supports our FRAP data, consistent with stabilization of SMII filaments upon agonist stimulation (Figure 4). While we find this myosin-centric model appealing, nonmutually exclusive models include stabilization by binding partners, such as caldesmon.[46] Future studies that extend our dynamic imaging of SMII to include dynamic imaging of MLCK, caldesmon, and more key players should help tease apart these models.

The idea that SMII can exist as an inactive filament with relatively low RLC phosphorylation, like striated myosin 2s, but can be induced to rapidly assemble nascent filaments upon stimulation, like nonmuscle myosin 2s, suggests that SMII is somewhat of a hybrid of its myosin 2 paralogs. While we have a working model for how rapid assembly might occur via RLC phosphorylation of 10S monomers, described above, we have a less clear structural model of how SMII exists as an inactive filament. One possibility can be derived from studies in striated myosin 2s, where filamentous myosin 2 monomers can exist in a sequestered state, in which the motor domains dock on one another and fold back toward the proximal tail.[47,48] This interacting-heads motif (IHM) was actually first discovered in SMII and is a stabilizing feature of the folded 10S monomer.[47–49] However, the IHM has not been directly observed in filamentous SMII, only in the folded monomer. Detailed analyses of the striated IHM have been enabled by the crystalline nature of striated filaments and advances in structural biology (ie, cryo-EM).[50,51] It is possible that the less ordered nature of SMII filaments in SMCs precludes filamentous IHM detection in cells, or a requisite stabilizing binding partner precludes filamentous IHM detection in vitro. Whether SMII also adopts a filamentous IHM state, therefore, remains an open question.

Extracting more molecular-level assembly information from our FRAP data during induced contraction is challenged by the timescales at play. In our experiments, cytosolic calcium, SMII assembly, and traction forces all peak within 1 to 2 minutes of carbachol-/angII-induced activation, after which they decay to steady-state levels within minutes (Figure 3). However, plateaus in our carbachol-treated FRAP data (required to fit exponential curves) require observation for ≈5 to 10 minutes (Figures 4 and 6). Therefore, the SMII networks in the bleach regions are likely experiencing exchange while simultaneously undergoing concurrent assembly and disassembly during the acquisition, complicating interpretation of a first exponential kinetic model. To address this, we quantified terminal mean intensity and curve type (exponential, linear, or minimal recovery), and we observed a consistent decrease in end point recovery following agonist exposure, suggesting stabilization and a reduced exchangeable pool even in cells that could not be fit exponentially. This analysis provides a conservative readout of stabilization that complements mobile fraction estimates derived from exponential curves. Future experiments with higher temporal resolution (eg, single-molecule tracking of SMII incorporation lifetimes) should more fully elucidate changes in exchange kinetics throughout an induced contraction event.

The observation that SMII and NM2 are likely coassembling in filaments is not unexpected, as we know that NM2 isoforms coassemble with one another, and SMII and NM2 isoforms share high sequence and structure similarities.[24,52] While NM2 is expressed in many SMCs,[30] SMII expression is dominant over NM2.[53] Therefore, the fraction of NM2 in mixed NM2:SMII filaments is likely low. Interestingly, in vitro experiments analyzing the processive movement of purified NM2 filaments demonstrated that adding a fraction (≈30%) of the NM2B isoform into filaments of the NM2A isoform was sufficient to completely render the filament NM2B-like.[54] Therefore, biophysical properties of myosin 2 filaments are not linearly derived from their isoform composition, and a fraction of NM2 could meaningfully contribute to SMII filaments. Previous studies have implicated NM2 function in SMCs.[55,56] However, it is difficult to discern if any potential NM2 functionality is due to NM2 coassembling into SMII filaments or behaving independently. Future studies selectively ablating NM2 isoforms in smooth muscle tissues or performing

mixed in vitro experiments similar to previous studies with NM2 isoforms[54] to determine the biophysical properties of mixed NM2:SMII filaments should prove insightful.

Further complicating SMII and NM2 coassembly is the presence of SMII splice variants in each SMC population[57] that could further contribute to variations in contractile properties. While in vitro studies have suggested that these isoforms display unique assembly properties,[58] future studies might explore exchange kinetics of SMII isoforms in cells and correlations with contractile properties of the SMCs in which the isoforms are expressed. Additional complexity could also arise from heterogeneous myosin 2 subcellular functions within SMCs, as recent evidence demonstrated unique subcellular localization for SMII and NM2 in freshly isolated primary cells.[59] Finally, while the structure of NM2 bipolar filaments in cells is relatively well-established, the precise structural features of SMII filaments in intact cells and tissues (ie, side-polar filaments) remain an active area of debate.[60] Dissecting the unique and common biophysical properties of SMII and NM2 filaments in SMCs will likely yield important insights.

How might altered SMII assembly and exchange contribute to vascular disease? Vascular SMCs must perform different roles across the arterial tree: in large elastic arteries such as the aorta, SMCs are integrated into elastin-contractile units that help maintain wall architecture and compliance,[61,62] whereas, in resistance arteries, acute changes in SMC contractile state regulate vessel diameter, peripheral resistance, and local tissue perfusion.[63] The ability to rapidly tune force production via SMII modulation could enable rapid tuning of vascular tone or blood pressure to a new setpoint, and inability to do so could initiate or potentiate pathology.[64] Our findings suggest that disease-associated changes in SMC stiffness, vascular tone, and wall mechanics may arise not only from altered myosin activation or actin organization, as has been observed in hypertensive rats,[65] but also from changes in SMII filament assembly and exchange. Failure to assemble or stabilize SMII filaments during agonist stimulation could reduce necessary contractile reserve and weaken the SMC contribution to vessel wall mechanics, a possible mechanism in *MYH11*-associated thoracic aortic aneurysm and dissection. Conversely, excessive or prolonged SMII stabilization could favor increased basal tone, arterial stiffness, or maladaptive vasoconstriction. Phenotypic switching, inflammatory signaling, altered MLCK/RhoA/ROCK activity, and variants that affect 10S/IHM stability or coiled-coil filament assembly (discussed below) could each shift this balance. Thus, SMII filament dynamics are not merely a physiological mechanism of SMCs but likely a measurable regulatory layer through which SMCs may tune vascular mechanics in health and disease. In addition, SMII filament dynamics may be a functional readout for future studies of *MYH11* variants, vascular disease models, and therapies that alter myosin activation or cytoskeletal stability. This concept can be extended well beyond vascular smooth muscle to smooth muscle throughout the body. For example, gastrointestinal smooth muscle performs phasic contraction to move food through the gastrointestinal tract,[66] where SMII dynamics are almost certainly contributing to both physiology and pathophysiology, and studies in airway SMCs have demonstrated stretch-induced actomyosin filament dynamics.[67,68]

In addition to SMII acting within a disease state, pathogenic and likely pathogenic variants in *MYH11* can drive vascular and gastrointestinal disorders, including familial aortic aneurysm and dissection.[4,5] However, most of these variants have not received mechanistic scrutiny. In contrast, recent advances in cardiomyopathy-driving myosin variants (primarily *MYH7*) suggest that some mutations are either stabilizing or destabilizing the IHM to create hypocontractile or hypercontractile systems.[69] Some pathogenic variants in the NM2A heavy chain, collectively termed *MYH9*-related disease, occur in the coiled-coil tail and are thought to disrupt filament assembly and dynamics.[70,71] Identifying how these variants impact SMII dynamics could, therefore, inform our understanding of the pathologies they are tied to.

Overall, our studies provide foundational insight into SMC physiology by establishing that SMII filaments are both predominantly filament-associated and dynamically exchanging at baseline, and agonist stimulation induces filament assembly and stabilization, alongside motor activation to produce force. By extending these measurements from an immortalized cell culture model to primary SMCs and intact arterioles at endogenous expression, our studies open the door to elucidating precise and unexplored mechanisms (eg, heavy chain phosphorylation and differential MLCK signaling) for both normal physiology and pathophysiology.

ARTICLE INFORMATION

Received April 23, 2026; accepted June 25, 2026.

Affiliation

Department of Cell and Molecular Physiology, Stritch School of Medicine, Loyola University Chicago, Maywood, IL. Now with Department of Medicine, Section of Cardiology, University of Chicago, IL (J.A.K.).

Acknowledgments

The authors thank Drs Ivana Kuo and Quan Cao, and the Loyola University Chicago Cardiovascular Research Institute for echocardiography and blood pressure measurements. The authors thank the Transgenic Animal Facility at the University of Chicago and the Loyola University Chicago Imaging Facility for core support.

Author Contributions

M.A. Bennett, S.K. Demeulenaere, P.W. Oakes, and J.R. Beach developed the project. S.K. Demeulenaere, M.A. Bennett, B. Somerfield, H. Wu, M.E. Utgaard, S. Sala, H. Patel, E.R. Longtine, and J.R. Beach performed experiments. S.K. Demeulenaere, M.A. Bennett, B. Somerfield, H. Wu, A. Zied, J.A. Kirk, and J.R. Beach generated critical reagents. S.K. Demeulenaere, M.A. Bennett, B. Somerfield, P.W. Oakes, and J.R. Beach analyzed the data. S.K. Demeulenaere, M.A. Bennett, P.W. Oakes, and J.R. Beach wrote the initial manuscript. All authors edited and approved the final text.

Sources of Funding

This work was supported in part by the National Institutes of Health grants R35-GM138183 to J.R. Beach, R01-GM148644 to P.W. Oakes, F30-HL178288 to S.K. Demeulenaere, LUC Transformative Research Pilot Grant to J.R. Beach and P.W. Oakes, and shared instrument grants to LUC for Zeiss SIM5 (S10OD034431) and transthoracic echocardiography equipment (S10OD028449).

Disclosures

None.

Supplemental Material

Figures S1–S9
Major Resources Table

REFERENCES

1. Zhuge Y, Zhang J, Qian F, Wen Z, Niu C, Xu K, Ji H, Rong X, Chu M, Jia C. Role of smooth muscle cells in cardiovascular disease. *Int J Biol Sci*. 2020;16:2741–2751. doi: 10.7150/ijbs.49871
2. Panner BJ, Honig CR. Filament ultrastructure and organization in vertebrate smooth muscle. Contraction hypothesis based on localization of actin and myosin. *J Cell Biol*. 1967;35:303–321. doi: 10.1083/jcb.35.2.303
3. Takeda N, Komuro I. Genetic basis of hereditary thoracic aortic aneurysms and dissections. *J Cardiol*. 2019;74:136–143. doi: 10.1016/j.jjcc.2019.03.014
4. Pannu H, Tran-Fadulu V, Papke CL, Scherer S, Liu Y, Presley C, Guo D, Estrera AL, Safi HJ, Brasier AR, et al. MYH11 mutations result in a distinct vascular pathology driven by insulin-like growth factor 1 and angiotensin II. *Hum Mol Genet*. 2007;16:2453–2462. doi: 10.1093/hmg/ddm201
5. Zhu L, Vranckx R, Khau Van Kien P, Lalande A, Boisset N, Mathieu F, Wegman M, Glancy L, Gasc J-M, Brunotte F, et al. Mutations in myosin heavy chain 11 cause a syndrome associating thoracic aortic aneurysm/aortic dissection and patent ductus arteriosus. *Nat Genet*. 2006;38:343–349. doi: 10.1038/ng1721
6. Hartman MA, Spudich JA. The myosin superfamily at a glance. *J Cell Sci*. 2012;125:1627–1632. doi: 10.1242/jcs.094300
7. Squire JM. General model for the structure of all myosin-containing filaments. *Nature*. 1971;233:457–462. doi: 10.1038/233457a0
8. Squire JM. Muscle myosin filaments: cores, crowns and couplings. *Biophys Rev*. 2009;1:149. doi: 10.1007/s12551-009-0017-4
9. Ikebe M, Hartshorne DJ, Elzinga M. Identification, phosphorylation, and dephosphorylation of a second site for myosin light chain kinase on the 20,000-dalton light chain of smooth muscle myosin. *J Biol Chem*. 1986;261:36–39. doi: 10.1016/S0021-9258(17)42425-2
10. Sellers JR, Pato MD, Adelstein RS. Reversible phosphorylation of smooth muscle myosin, heavy meromyosin, and platelet myosin. *J Biol Chem*. 1981;256:13137–13142. doi: 10.1016/S0021-9258(18)43018-9
11. Corson MA, Sellers JR, Adelstein RS, Schoenberg M. Substance P contracts bovine tracheal smooth muscle via activation of myosin light chain kinase. *Am J Physiol*. 1990;259:C258–C265. doi: 10.1152/ajpcell.1990.259.2.C258
12. Breckenridge MT, Dulyaninova NG, Egelhoff TT. Multiple regulatory steps control mammalian nonmuscle myosin II assembly in live cells. *Mol Biol Cell*. 2009;20:338–347. doi: 10.1091/mbc.e08-04-0372
13. Vicente-Manzanares M, Zareno J, Whitmore L, Choi CK, Horwitz AF. Regulation of protrusion, adhesion dynamics, and polarity by myosins IIA and IIB in migrating cells. *J Cell Biol*. 2007;176:573–580. doi: 10.1083/jcb.200612043
14. Wood NB, Kelly CM, O'Leary TS, Martin JL, Previs MJ. Cardiac myosin filaments are maintained by stochastic protein replacement. *Mol Cell Proteomics*. 2022;21:100274. doi: 10.1016/j.mcpro.2022.100274
15. Seow CY. Myosin filament assembly in an ever-changing myofilament lattice of smooth muscle. *Am J Physiol Cell Physiol*. 2005;289:C1363–C1368. doi: 10.1152/ajpcell.00329.2005
16. Wang L, Chitano P, Seow CY. Filament evanescence of myosin II and smooth muscle function. *J Gen Physiol*. 2021;153:e202012781. doi: 10.1085/jgp.202012781
17. Webb RC. Smooth muscle contraction and relaxation. *Adv Physiol Educ*. 2003;27:201–206. doi: 10.1152/advan.00025.2003
18. Chitano P, Wang L, Tin GYY, Ikebe M, Paré PD, Seow CY. Smooth muscle function and myosin polymerization. *J Cell Sci*. 2017;130:2468–2480. doi: 10.1242/jcs.202812
19. Milton DL, Schneck AN, Ziech DA, Ba M, Facemyer KC, Halayko AJ, Baker JE, Gerthoffer WT, Cremo CR. Direct evidence for functional smooth muscle myosin II in the 10S self-inhibited monomeric conformation in airway smooth muscle cells. *Proc Natl Acad Sci USA*. 2011;108:1421–1426. doi: 10.1073/pnas.1011784108
20. Cao G, Xuan X, Hu J, Zhang R, Jin H, Dong H. How vascular smooth muscle cell phenotype switching contributes to vascular disease. *Cell Commun Signal*. 2022;20:180. doi: 10.1186/s12964-022-00993-2
21. Chen R, McVey DG, Shen D, Huang X, Ye S. Phenotypic switching of vascular smooth muscle cells in atherosclerosis. *J Am Heart Assoc*. 2023;12:e031121. doi: 10.1161/JAHA.123.031121
22. Jensen LF, Bentzon JF, Albarrán-Juárez J. The phenotypic responses of vascular smooth muscle cells exposed to mechanical cues. *Cells*. 2021;10:2209. doi: 10.3390/cells10092209
23. Owens GK, Kumar MS, Wamhoff BR. Molecular regulation of vascular smooth muscle cell differentiation in development and disease. *Physiol Rev*. 2004;84:767–801. doi: 10.1152/physrev.00041.2003
24. Beach JR, Shao L, Remmert K, Li D, Betzig E, Hammer JA 3rd. Nonmuscle myosin II isoforms coassemble in living cells. *Curr Biol*. 2014;24:1160–1166. doi: 10.1016/j.cub.2014.03.071
25. Miano JM, Fisher EA, Majesky MW. Fate and state of vascular smooth muscle cells in atherosclerosis. *Circulation*. 2021;143:2110–2116. doi: 10.1161/CIRCULATIONAHA.120.049922
26. Rademacher DJ, Cabe M, Bakowska JC. Fluorescence recovery after photobleaching of yellow fluorescent protein tagged p62 in aggresome-like induced structures. *J Vis Exp*. 2019:145. doi: 10.3791/59288
27. Sabass B, Gardel ML, Waterman CM, Schwarz US. High resolution traction force microscopy based on experimental and computational advances. *Biophys J*. 2008;94:207–220. doi: 10.1529/biophysj.107.113670
28. Schmitt MS, Colen J, Sala S, Devany J, Seetharaman S, Caillier A, Gardel ML, Oakes PW, Vitelli V. Machine learning interpretable models of cell mechanics from protein images. *Cell*. 2024;187:481–494.e24. doi: 10.1016/j.cell.2023.11.041
29. Oakes PW, Banerjee S, Marchetti MC, Gardel ML. Geometry regulates traction stresses in adherent cells. *Biophys J*. 2014;107:825–833. doi: 10.1016/j.bpj.2014.06.045
30. Eddinger TJ, Meer DP. Myosin II isoforms in smooth muscle: heterogeneity and function. *Am J Physiol Cell Physiol*. 2007;293:C493–C508. doi: 10.1152/ajpcell.00131.2007
31. White SL, Zhou MY, Low RB, Periasamy M. Myosin heavy chain isoform expression in rat smooth muscle development. *Am J Physiol*. 1998;275:C581–C589. doi: 10.1152/ajpcell.1998.275.2.C581
32. DiSanto ME, Cox RH, Wang Z, Chacko S. NH2-terminal-inserted myosin II heavy chain is expressed in smooth muscle of small muscular arteries. *Am J Physiol*. 1997;272:C1532–C1542. doi: 10.1152/ajpcell.1997.272.5.C1532
33. Ojima K, Ichimura E, Yasukawa Y, Wakamatsu JI, Nishimura T. Dynamics of myosin replacement in skeletal muscle cells. *Am J Physiol Cell Physiol*. 2015;309:C669–C679. doi: 10.1152/ajpcell.00170.2015
34. Tang DD. The dynamic actin cytoskeleton in smooth muscle. *Adv Pharmacol*. 2018;81:1–38. doi: 10.1016/bs.apha.2017.06.001
35. Rovner AS, Murphy RA, Owens GK. Expression of smooth muscle and nonmuscle myosin heavy chains in cultured vascular smooth muscle cells. *J Biol Chem*. 1986;261:14740–14745. doi: 10.1016/S0021-9258(18)66933-9
36. Quintanilla MA, Hammer JA, Beach JR. Non-muscle myosin 2 at a glance. *J Cell Sci*. 2023;136:jcs260890. doi: 10.1242/jcs.260890
37. Satoh H. Modulation of Ca2+-activated K+ current by isoprenaline, carbachol, and phorbol ester in cultured (and fresh) rat aortic vascular smooth muscle cells. *Gen Pharmacol*. 1996;27:319–324. doi: 10.1016/0306-3623(95)02005-5
38. Wu K, Patel H, Wu H, Demeulenaere SK, Patel V, Utgaard M, Quintanilla MA, Bennett MA, Sala S, Beach JR. Nonmuscle myosin 2 without an assembly competence domain can incorporate into established filaments in cells. *Mol Biol Cell*. 2025;36:ar95. doi: 10.1091/mbc.E24-07-0287
39. Isotani E, Zhi G, Lau KS, Huang J, Mizuno Y, Persechini A, Geguchadze R, Kamm KE, Stull JT. Real-time evaluation of myosin light chain kinase activation in smooth muscle tissues from a transgenic calmodulin-biosensor mouse. *Proc Natl Acad Sci USA*. 2004;101:6279–6284. doi: 10.1073/pnas.0308742101
40. Alexander RW, Brock TA, Gimbrone MA, Rittenhouse SE. Angiotensin increases inositol trisphosphate and calcium in vascular smooth muscle. *Hypertension*. 1985;7:447–451
41. Kimes BW, Brandt BL. Characterization of two putative smooth muscle cell lines from rat thoracic aorta. *Exp Cell Res*. 1976;98:349–366. doi: 10.1016/0014-4827(76)90446-8
42. Adelstein RS, Conti MA. Phosphorylation of platelet myosin increases actin-activated myosin ATPase activity. *Nature*. 1975;256:597–598. doi: 10.1038/256597a0

43. Rovner AS, Fagnant PM, Trybus KM. Phosphorylation of a single head of smooth muscle myosin activates the whole molecule. *Biochemistry*. 2006;45:5280–5289. doi: 10.1021/bi060154c
44. Walcott S, Fagnant PM, Trybus KM, Warshaw DM. Smooth muscle heavy meromyosin phosphorylated on one of its two heads supports force and motion. *J Biol Chem*. 2009;284:18244–18251. doi: 10.1074/jbc.M109.003293
45. Somlyo AV, Butler TM, Bond M, Somlyo AP. Myosin filaments have non-phosphorylated light chains in relaxed smooth muscle. *Nature*. 1981;294:567–569. doi: 10.1038/294567a0
46. Marston S, Pinter K, Bennett P. Caldesmon binds to smooth muscle myosin and myosin rod and crosslinks thick filaments to actin filaments. *J Muscle Res Cell Motil*. 1992;13:206–218. doi: 10.1007/BF01874158
47. Wendt T, Taylor D, Messier T, Trybus KM, Taylor KA. Visualization of head-head interactions in the inhibited state of smooth muscle myosin. *J Cell Biol*. 1999;147:1385–1390. doi: 10.1083/jcb.147.7.1385
48. Wendt T, Taylor D, Trybus KM, Taylor K. Three-dimensional image reconstruction of dephosphorylated smooth muscle heavy meromyosin reveals asymmetry in the interaction between myosin heads and placement of subfragment 2. *Proc Natl Acad Sci USA*. 2001;98:4361–4366. doi: 10.1073/pnas.071051098
49. Heissler SM, Arora AS, Billington N, Sellers JR, Chinthalapudi K. Cryo-EM structure of the autoinhibited state of myosin-2. *Sci Adv*. 2021;7:eabk3273. doi: 10.1126/sciadv.abk3273
50. Grinzato A, Auguin D, Kikuti C, Nandwani N, Moussaoui D, Pathak D, Kandiah E, Ruppel KM, Spudich JA, Houdusse A, et al. Cryo-EM structure of the folded-back state of human β-cardiac myosin. *Nat Commun*. 2023;14:3166. doi: 10.1038/s41467-023-38698-w
51. Dutta D, Nguyen V, Campbell KS, Padrón R, Craig R. Cryo-EM structure of the human cardiac myosin filament. *Nature*. 2023;623:853–862. doi: 10.1038/s41586-023-06691-4
52. Shutova MS, Spessott WA, Giraudo CG, Svitkina T. Endogenous species of mammalian nonmuscle myosin IIA and IIB include activated monomers and heteropolymers. *Curr Biol*. 2014;24:1958–1968. doi: 10.1016/j.cub.2014.07.070
53. Gaylinn BD, Eddinger TJ, Martino PA, Monical PL, Hunt DF, Murphy RA. Expression of nonmuscle myosin heavy and light chains in smooth muscle. *Am J Physiol*. 1989;257:C997–1004. doi: 10.1152/ajpcell.1989.257.5.C997
54. Melli L, Billington N, Sun SA, Bird JE, Nagy A, Friedman TB, Takagi Y, Sellers JR. Bipolar filaments of human nonmuscle myosin 2-A and 2-B have distinct motile and mechanical properties. *Elife*. 2018;7:e32871. doi: 10.7554/eLife.32871
55. Morano I, Chai GX, Baltas LG, Lamounier-Zepter V, Lutsch G, Kott M, Haase H, Bader M. Smooth-muscle contraction without smooth-muscle myosin. *Nat Cell Biol*. 2000;2:371–375. doi: 10.1038/35014065
56. Zhang W, Gunst SJ. Non-muscle (NM) myosin heavy chain phosphorylation regulates the formation of NM myosin filaments, adhesome assembly and smooth muscle contraction. *J Physiol*. 2017;595:4279–4300. doi: 10.1113/JP273906
57. Hamada Y, Yanagisawa M, Katsuragawa Y, Coleman JR, Nagata S, Matsuda G, Masaki T. Distinct vascular and intestinal smooth muscle myosin heavy chain mRNAs are encoded by a single-copy gene in the chicken. *Biochem Biophys Res Commun*. 1990;170:53–58. doi: 10.1016/0006-291x(90)91239-o
58. Rovner AS, Fagnant PM, Lowey S, Trybus KM. The carboxyl-terminal isoforms of smooth muscle myosin heavy chain determine thick filament assembly properties. *J Cell Biol*. 2002;156:113–123. doi: 10.1083/jcb.200107131
59. Singh K, Kim AB, Morgan KG. Non-muscle myosin II regulates aortic stiffness through effects on specific focal adhesion proteins and the non-muscle cortical cytoskeleton. *J Cell Mol Med*. 2021;25:2471. doi: 10.1111/jcmm.16170
60. Sobieszek IJ, Sobieszek A. Myosin assembly of smooth muscle: from ribbons and side polarity to a row polar helical model. *J Muscle Res Cell Motil*. 2022;43:113–133. doi: 10.1007/s10974-022-09622-4
61. Wolinsky H, Glagov S. Structural basis for the static mechanical properties of the aortic media. *Circ Res*. 1964;14:400–413. doi: 10.1161/01.res.14.5.400
62. Karimi A, Milewicz DM. Structure of the elastin-contractile units in the thoracic aorta and how genes that cause thoracic aortic aneurysms and dissections disrupt this structure. *Can J Cardiol*. 2016;32:26–34. doi: 10.1016/j.cjca.2015.11.004
63. Mulvany MJ, Halpern W. Contractile properties of small arterial resistance vessels in spontaneously hypertensive and normotensive rats. *Circ Res*. 1977;41:19–26. doi: 10.1161/01.res.41.1.19
64. Milewicz DM, Trybus KM, Guo DC, Sweeney HL, Regalado E, Kamm K, Stull JT. Altered smooth muscle cell force generation as a driver of thoracic aortic aneurysms and dissections. *Arterioscler Thromb Vasc Biol*. 2017;37:26–34. doi: 10.1161/ATVBAHA.116.303229
65. Sehgel NL, Zhu Y, Sun Z, Trzeciakowski JP, Hong Z, Hunter WC, Vatner DE, Meininger GA, Vatner SF. Increased vascular smooth muscle cell stiffness: a novel mechanism for aortic stiffness in hypertension. *Am J Physiol Heart Circ Physiol*. 2013;305:H1281–H1287. doi: 10.1152/ajpheart.00232.2013
66. Bayliss WM, Starling EH. The movements and innervation of the small intestine. *J Physiol*. 1899;24:99–143. doi: 10.1113/jphysiol.1899.sp000752
67. Kuo KH, Wang L, Paré PD, Ford LE, Seow CY. Myosin thick filament lability induced by mechanical strain in airway smooth muscle. *J Appl Physiol*. 2001;90:1811–1816. doi: 10.1152/jappl.2001.90.5.1811
68. Lan B, Krishnan R, Park CY, Watanabe RA, Panganiban R, Butler JP, Lu Q, Cole WC, Fredberg JJ. Transient stretch induces cytoskeletal fluidization through the severing action of cofilin. *Am J Physiol Lung Cell Mol Physiol*. 2018;314:L799–L807. doi: 10.1152/ajplung.00326.2017
69. Alamo L, Ware JS, Pinto A, Gillilan RE, Seidman JG, Seidman CE, Padrón R. Effects of myosin variants on interacting-heads motif explain distinct hypertrophic and dilated cardiomyopathy phenotypes. *Elife*. 2017;6:e24634. doi: 10.7554/eLife.24634
70. Kelley MJ, Jawien W, Ortel TL, Korczak JF. Mutation of MYH9, encoding non-muscle myosin heavy chain A, in May-Hegglin anomaly. *Nat Genet*. 2000;26:106–108. doi: 10.1038/79069
71. Pal K, Nowak R, Billington N, Liu R, Ghosh A, Sellers JR, Fowler VM. Megakaryocyte migration defects due to nonmuscle myosin IIA mutations underly thrombocytopenia in MYH9-Related Disease. *Blood*. 2020;135:1887–1898. doi: 10.1182/blood.2019003064